Electronic Supplementary Material (ESI) for Journal of Materials Chemistry A.

Enhancing the thermoelectric performance of $Sb_2Si_2Te_6$ by germanium doping

Weihua Wang[a,b], Xiaowei Lu[a], Lin Sun[a], Jipeng Luo[c], Quan Shi[c], Na Ta[a], Peng Jiang*[a,c], Xinhe Bao*[a,c]

[a] State Key Laboratory of Catalysis, CAS Center for Excellence in Nanoscience, Dalian Institute of Chemical Physics, Chinese Academy of Sciences, Dalian 116023, Liaoning, China

[b] University of Chinese Academy of Sciences, Beijing 100049, China

[c] Dalian National Laboratory for Clean Energy, Dalian Institute of Chemical Physics, Chinese Academy of Sciences, Dalian 116023, Liaoning, China

E-mail address: pengjiang@dicp.ac.cn (P. Jiang), xhbao@dicp.ac.cn (X. Bao).

1. Heat capacity *C*p of $Sb_2Si_{1.94}Ge_{0.06}Te_6$

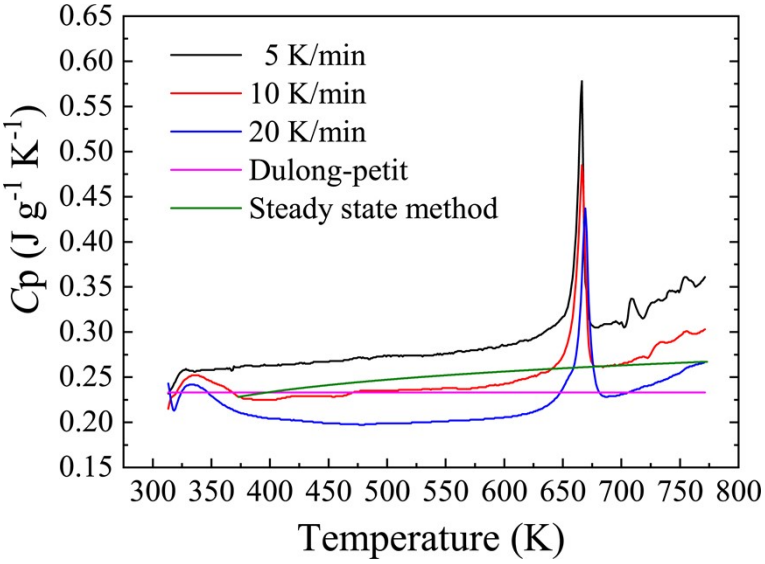

Fig. S1 Comparison of the specific heat capacity measured with different heating rates for differential scanning calorimeter (DSC), the quasi-steady state method and the Dulong-Petit theoretical value. Such comparison suggests that the heating rate of 10 K/min for DSC measurement provides the most reliable values.

2. In-situ X-ray diffraction

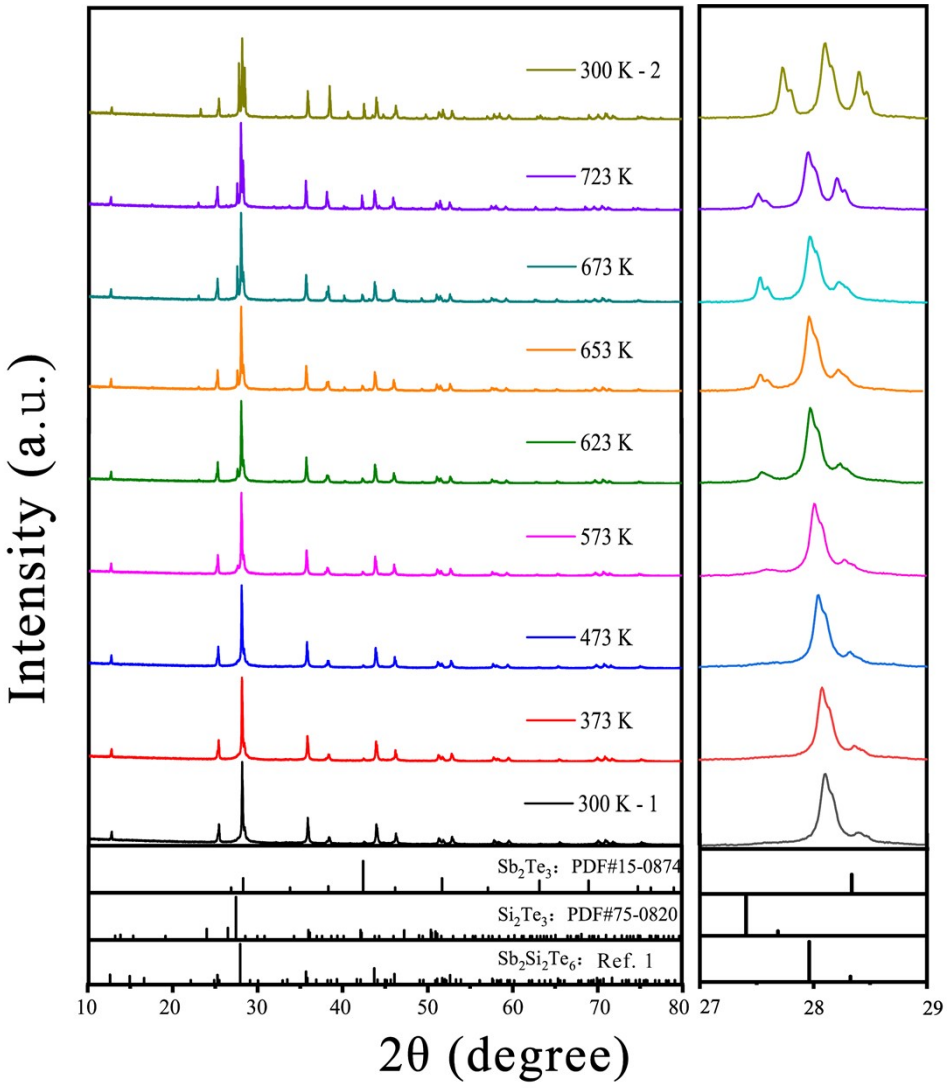

Fig. S2 In-situ X-ray diffraction patterns of the $Sb_2Si_2Te_6$. 300 K-1 and 300 K-2 correspond to the room-temperature results of the original sample and the sample after heating process, respectively.

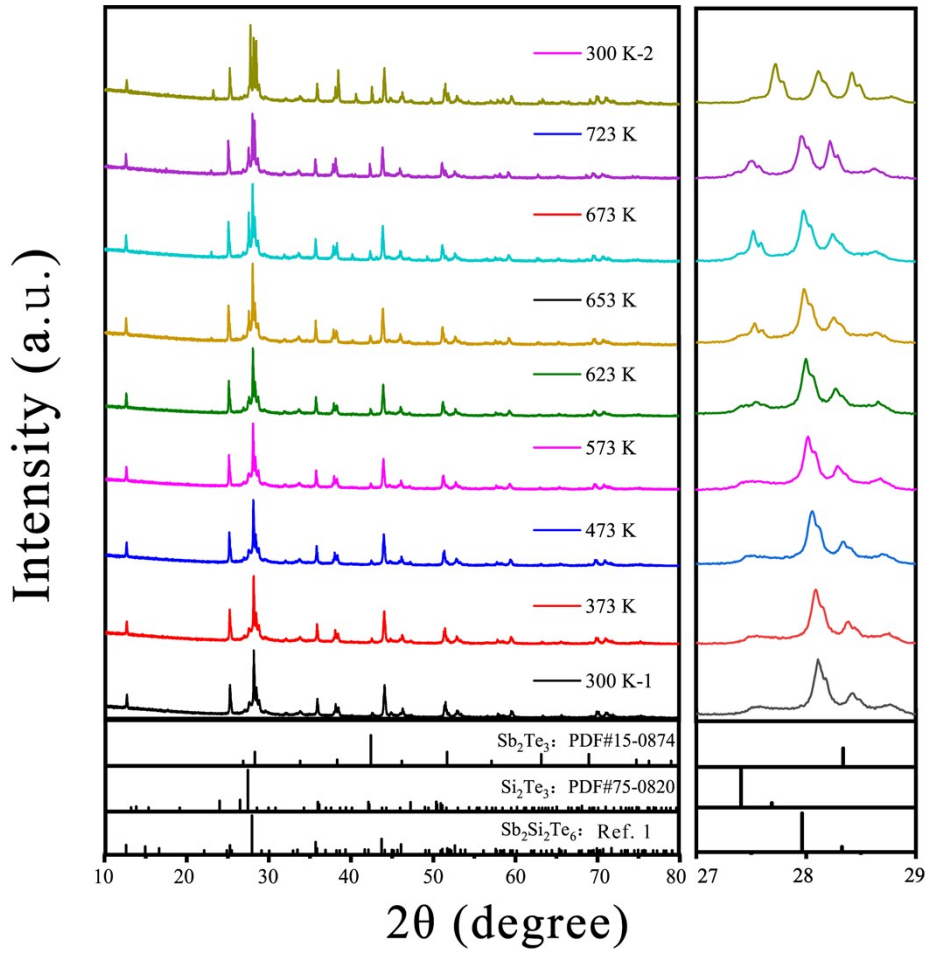

Fig. S3 In-situ X-ray diffraction patterns of the $Sb_2Si_{1.94}Ge_{0.06}Te_6$. 300 K-1 and 300 K-2 correspond to the room-temperature results of the original sample and the sample after heating process, respectively.

3. The isotropy of $Sb_2Si_{1.94}Ge_{0.06}Te_6$ thermoelectric performance

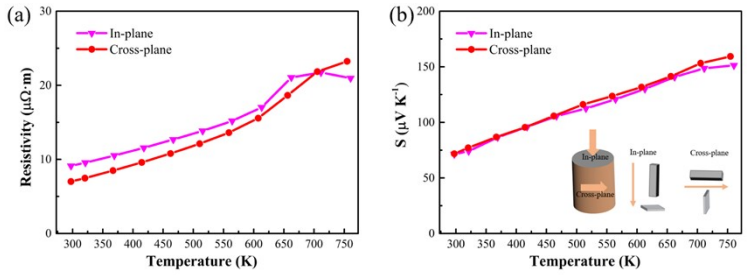

Fig. S4 Temperature-dependent (a) electrical resistivities and (b) Seebeck coefficients of $Sb_2Si_{1.94}Ge_{0.06}Te_6$ measured along different directions.

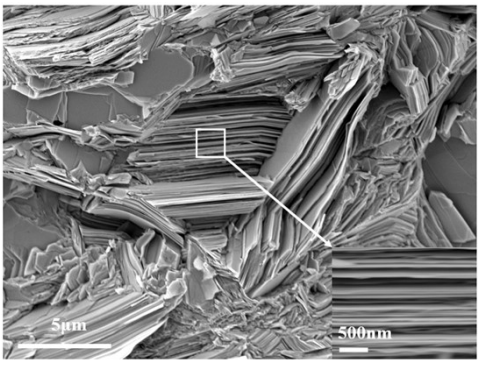

Fig. S5 The SEM images of the $Sb_2Si_2Te_6$ sample.

4. The reproducibility of experimental results

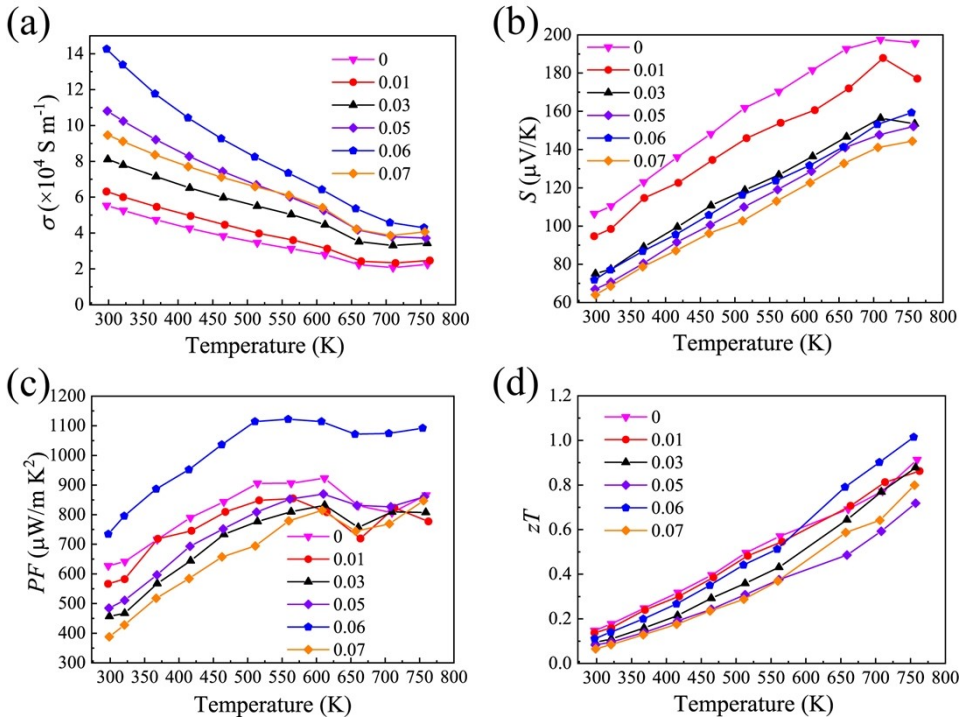

Fig. S6 Temperature dependence of thermoelectric properties of $Sb_2Si_{2-x}Ge_xTe_6$ (x=0, 0.01, 0.03, 0.05, 0.06, 0.07): (a) electrical resistivity, (b) Seebeck coefficient, (c) power factor, (d) zT values of $Sb_2Si_{2-x}Ge_xTe_6$. All samples were re-prepared using the same procedure.

5. Lattice thermal conductivity

The lattice thermal conductivity κ_{lat} is calculated from $\kappa_{lat} = \kappa_{tot} - \kappa_{car}$. Here the

carrier thermal conductivity κ_{car} is calculated by the Wiedemann-Franz law,[2,3] $\kappa_{car} = L\sigma T$, where L is the Lorenz number. The total thermal conductivity κ_{tot} is obtained by the equation $\kappa = D\rho C_p$.

Based on the single band approximation, the Seebeck coefficient can be described by formula (S1) and (S2), and the Lorenz number L can be calculated by equation (S3).

$$S = \pm \frac{k_B}{e}\left(\frac{(r+5/2)F_{r+3/2}(\xi)}{(r+3/2)F_{r+1/2}(\xi)} - \xi\right) \quad \text{S1}$$

$$F_n(\xi) = \int_0^\infty \frac{x^n}{1+e^{x-\xi}}dx \quad \text{S2}$$

$$L = \left(\frac{k_B}{e}\right)^2\left(\frac{(r+7/2)F_{r+5/2}(\xi)}{(r+3/2)F_{r+1/2}(\xi)} - \left[\frac{(r+5/2)F_{r+3/2}(\xi)}{(r+3/2)F_{r+1/2}(\xi)}\right]^2\right) \quad \text{S3}$$

where $F_n(\xi)$ is the nth order Fermi integration, ξ is the reduced Fermi energy, r is the scattering parameter, k_B is the Boltzmann's constant, x is the variable of integration, and e is the electron charge. Here, the acoustic phonon scattering has been assumed as the main carrier scattering mechanism, r = -0.5. By applying the calculated ξ into Equation (S3), the Lorenz number is obtained as shown in Fig. S6 (a). Combining the κ_{tot} in Fig. S6 (b), the κ_{lat} and κ_{car} can also be obtained (Fig. S6 (c) and Fig. S6 (d)). As shown in Fig. S6 (c) and Fig. S6 (d), $Sb_2Si_{1.94}Ge_{0.06}Te_6$ has the lowest lattice thermal conductivity and the highest carrier thermal conductivity. The reduction of κ_{lat} primarily can be ascribed to the phonon scattering.

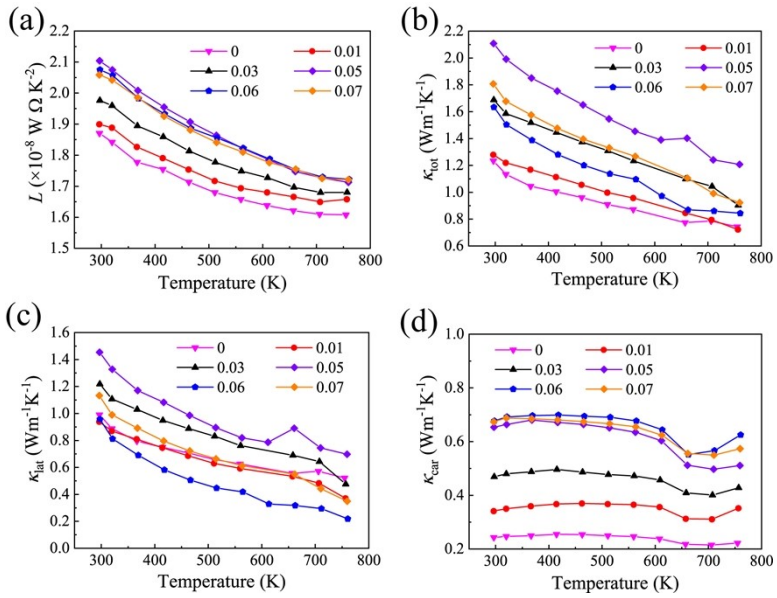

Fig. S7 Temperature-dependent (a) Lorenz constant, (b) total thermal conductivity, (c) lattice thermal conductivity, and (d) electronic thermal conductivity for $Sb_2Si_{2-x}Ge_xTe_6$ (x = 0, 0.01, 0.03, 0.05, 0.06, 0.07).

6. The thermal expansion coefficient measurement

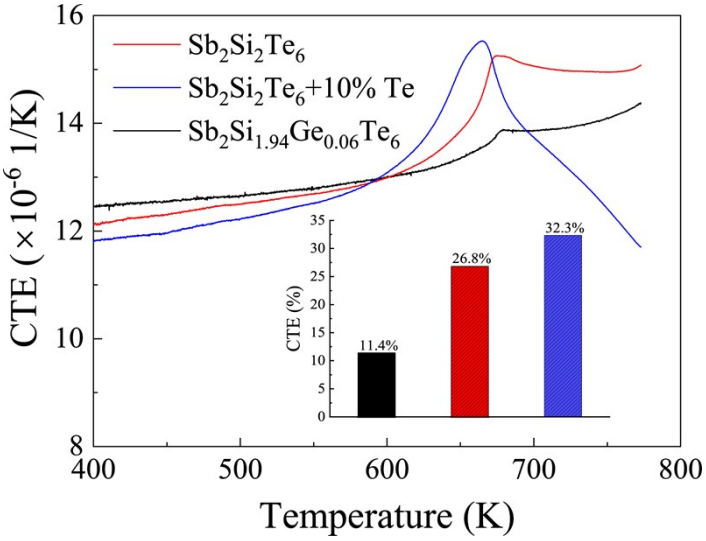

Fig. S8 The temperature dependent CTE of the $Sb_2Si_2Te_6$, $Sb_2Si_{1.94}Ge_{0.06}Te_6$ and $Sb_2Si_2Te_6$+10wt% Te. The insert shows the rate of CTE change from 373 K to the phase transition temperature of three samples.

7. Thermal cycling stability testing

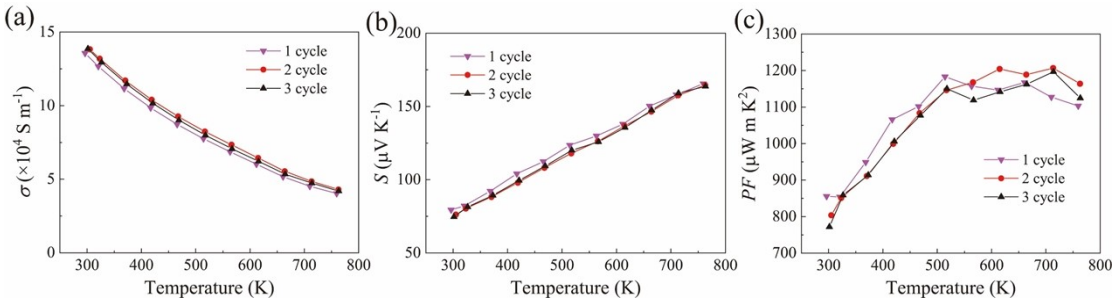

Fig. S9 The change of (a) electrical conductivity, (b) Seebeck coefficient and (c) power factor under three thermal cycles.

8. Three-dimensional numerical simulation model

All legs of the $Mg_{3.2}Sb_{1.5}Bi_{0.49}Te_{0.01}$ (n type) and $Sb_2Si_{1.94}Ge_{0.06}Te_6$ (p type) are set with the same cross-sectional area, 4 mm × 4 mm. The thickness of the copper electrode is 0.2 mm, and the thickness of the aluminum nitride ceramic plate is 0.5 mm.

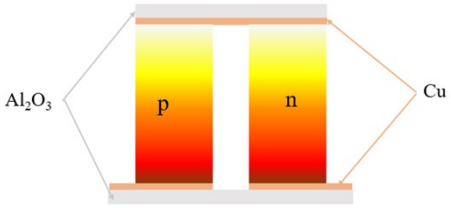

Fig. S10 Schematic diagram of the thermoelectric device.

9. Synthesis and properties of $Mg_{3.2}Sb_{1.5}Bi_{0.49}Te_{0.01}$

Polycrystalline $Mg_{3.2}Sb_{1.5}Bi_{0.49}Te_{0.01}$ samples were synthesized by high-energy milling magnesium scrap (99.8%, Damao Chemical Reagent Factory), antimony shots (99.99%, Lige Science), bismuth powder (99.99%, Aladdin) and Te shot (99.999%, ZhongNuo Advanced Material). They were sealed into stainless-steel vials according to stoichiometric ratios in an argon-filled glove box. The mixture was mechanically alloyed by high-energy ball milling with a high-energy mill (SPEX 8000D) for 1 h. The processed powder was loaded into a graphite die with 12.7 mm diameter and pressed by SPS for 10 min at 673 K and for 2 min at 1073 K under an axial pressure of 50 MPa.

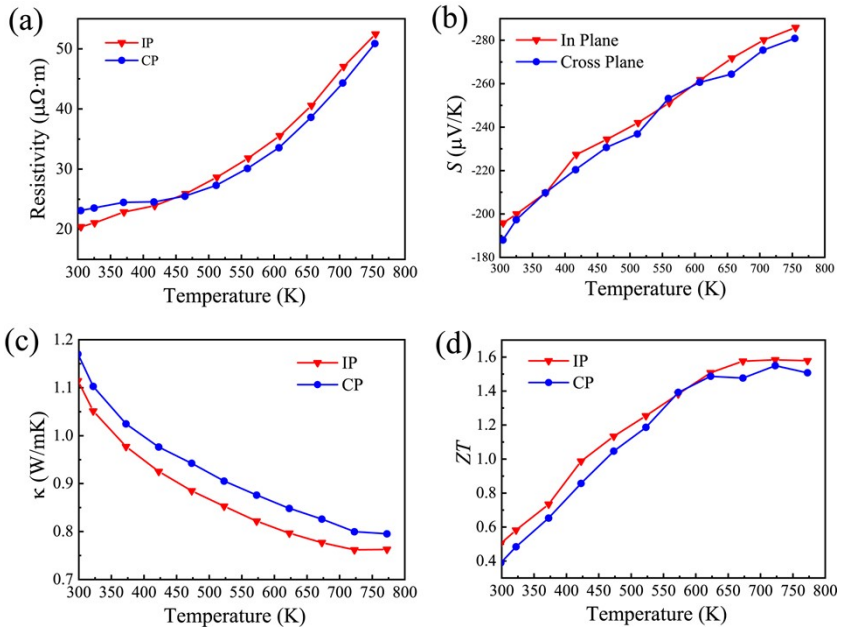

Fig. S11 The thermoelectric properties of the $Mg_{3.2}Sb_{1.5}Bi_{0.49}Te_{0.01}$ as a function of temperature along two directions.

10. Mechanical properties of $Sb_2Si_{1.94}Ge_{0.06}Te_6$ and $Mg_{3.2}Sb_{1.5}Bi_{0.49}Te_{0.01}$

Table S1 The mechanical properties of $Sb_2Si_{1.94}Ge_{0.06}Te_6$ and $Mg_{3.2}Sb_{1.5}Bi_{0.49}Te_{0.01}$

Materials	**CTE (×10^{-6} 1/K)**	**Compressive strength (MPa)**
$Sb_2Si_{1.94}Ge_{0.06}Te_6$	12 ─ 14	49
$Mg_{3.2}Sb_{1.5}Bi_{0.49}Te_{0.01}$	17.6 ─ 19.9	158

11. Geometrical optimization of the thermoelectric device

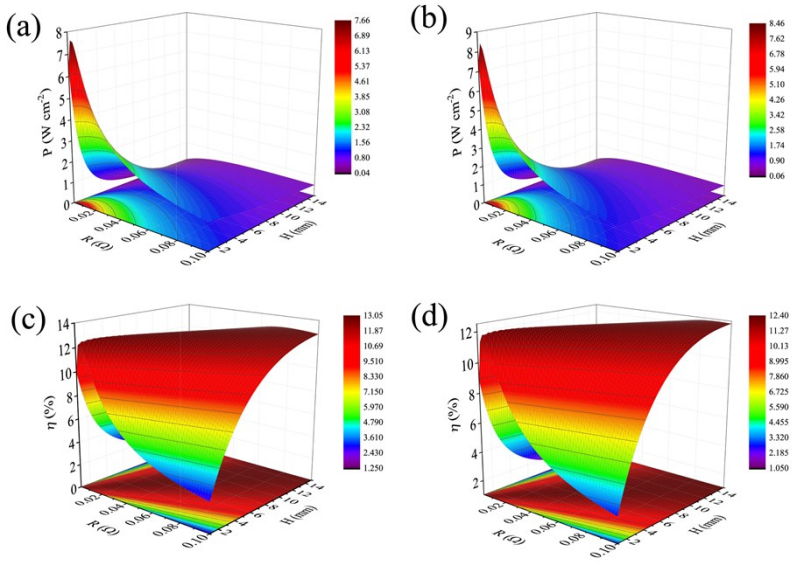

Fig. S12 The output power density (a and b) and the energy conversion efficiency (c and d) of the single pair thermoelectric module as a function of the height H of the p-type and n-type thermoelectric materials and the load resistance. The thermoelectric module is composed of n-type $Mg_{3.2}Sb_{1.5}Bi_{0.49}Te_{0.01}$ and p-type $Sb_2Si_2Te_6$ in (b) and (d) or $Sb_2Si_{1.94}Ge_{0.06}Te_6$ in (a) and (c). The thermoelectric performance of $Sb_2Si_2Te_6$ is from the literature.[1]

References

1 Y. B. Luo, S. T. Cai, S. Q. Hao, F. Pielnhofer, I. Hadar, Z. Z. Luo, J. W. Xu, C. Wolverton, V. P. Dravid, A. Pfitzner, Q. Y. Yan and M. G. Kanatzidis, *Joule*, 2020, **4**, 159–175.

2 W. S. Liu, Q. Y. Zhang, Y. C. Lan, S. Chen, X. Yan, Q. Zhang, H. Wang, D. Z. Wang, G. Chen, and Z. F. Ren, *Adv. Energy Mater.*, 2011, **1**, 577–587.

3 L. H. Huang, Q. Y. Zhang, Y. M. Wang, R. He, J. Shuai, J. J. Zhang, C. Wang, and Z. F. Ren, *Phys. Chem. Chem. Phys.*, 2017, **19**, 25683–25690.